Epitaxial Self-Assembly of Interfaces of 2D Metal−Organic Frameworks for Electroanalytical Detection of Neurotransmitters

Robert M. Stolz
Dartmouth College

Anna F. Kolin
Dartmouth College

Brunno C. Rocha
University of New Hampshire, Durham

Anna Brinks
Dartmouth College

Aileen M. Eagleton
Dartmouth College

See next page for additional authors.

Follow this and additional works at: https://scholars.unh.edu/nh_epscor

Comments

This is an Open Access article published by ACS Publications in ACS Nano in 2022, available online:

https://dx.doi.org/10.1021/acsnano.2c02529

Recommended Citation

Authors

Robert M. Stolz, Anna F. Kolin, Brunno C. Rocha, Anna Brinks, Aileen M. Eagleton, Lukasz Mendecki, Harish Vashisth, and Katherine A. Mirica

ARTICLE

Epitaxial Self-Assembly of Interfaces of 2D Metal–Organic Frameworks for Electroanalytical Detection of Neurotransmitters

Robert M. Stolz, Anna F. Kolln, Brunno C. Rocha, Anna Brinks, Aileen M. Eagleton, Lukasz Mendecki, Harish Vashisth, and Katherine A. Mirica*

Read Online

ACCESS | Metrics & More | Article Recommendations | SI Supporting Information

ABSTRACT: This paper identifies the electrochemical properties of individual facets of anisotropic layered conductive metal–organic frameworks (MOFs) based on $M_3(2,3,6,7,10,11$-hexahydroxytriphenylene$)_2$ $(M_3(HHTP)_2)$ (M = Co, Ni). The electroanalytical advantages of each facet are then applied toward the electrochemical detection of neurochemicals. By employing epitaxially controlled deposition of $M_3(HHTP)_2$ MOFs on electrodes, the contribution of the basal plane ({001} facets) and edge sites ({100} facets) of these MOFs can be individually determined using electrochemical characterization techniques. Despite having a lower observed heterogeneous electron transfer rate constant, the {001} facets of the $M_3(HHTP)_2$ systems prove more selective and sensitive for the detection of dopamine than the {100} facets of the same MOF, with the limit of detection (LOD) of 9.9 ± 2 nM in phosphate-buffered saline and 214 ± 48 nM in a simulated cerebrospinal fluid. Langmuir isotherm studies accompanied by all-atom MD simulations suggested that the observed improvement in performance and selectivity is related to the adsorption characteristics of analytes on the basal plane versus edge sites of the MOF interfaces. This work establishes that the distinct crystallographic facets of 2D MOFs can be used to control the fundamental interactions between analyte and electrode, leading to tunable electrochemical properties by controlling their preferential orientation through self-assembly.

KEYWORDS: metal−organic frameworks, conductive 2D materials, morphological control, electroanalysis, neurotransmitters, electrochemical Langmuir adsorption isotherms
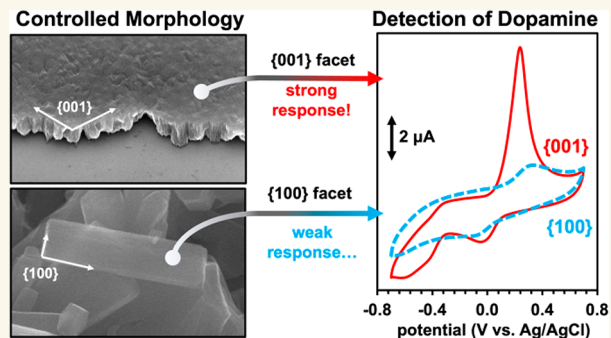
INTRODUCTION

Analytical electrochemistry is a powerful method that has revolutionized chemical detection in healthcare,[1] industry, and research.[2−4] Electrochemical methods have enabled advances in spatial resolution,[5] sensitivity,[6] and selectivity[7] in chemical analysis.[8,9] Among the most powerful and commonly used electroanalytical techniques, voltammetry (primarily cyclic voltammetry (CV), linear sweep voltammetry (LSV), square wave voltammetry (SWV), and differential pulse voltammetry (DPV)) has excelled due to its ability to differentiate and quantify analytes in solution rapidly and inexpensively.[10,11] These methods have proven to be amenable to miniaturization, integration into wireless sensors,[12,13] remote sensing applications,[14,15] and in vivo monitoring of biological processes.[16−18]

The development of materials for working electrodes has been a major driving force in advancing innovations in the design of electroanalytical devices.[19] For example, all known allotropes of carbon have been implemented as a component in working electrode systems for electrochemical detection of small molecules,[20] large biomolecules,[21−23] and ions in solution.[24−26] Sensing parameters of electrochemical systems have improved with the progression from naturally occurring graphitic materials to synthetic materials such as boron-doped diamond[27−30] and dimensionally controlled materials such as carbon nanotubes,[31,32] highly oriented pyrolytic graphite
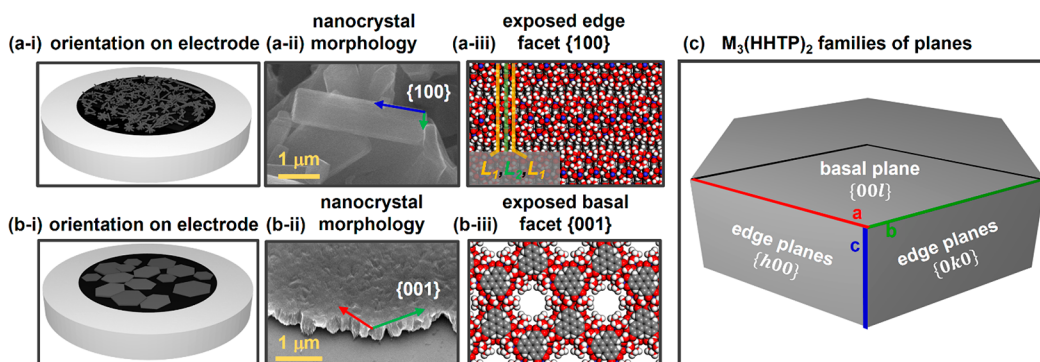
Figure 1. $M_3(HHTP)_2$ in the form of (a-i) hydrothermally grown and drop-casted MOF and (b-i) MOFs obtained by epitaxial growth and Langmuir−Blodgett deposition with their anticipated orientation on the electrode surface. Scanning electron micrographs of (a-ii) nanorods and (b-ii) nanosheets. Idealized models of exposed crystal facets belonging to the Bragg family of planes (a-iii) {100} or (b-iii) {001} were generated from reported crystal structures (blue: metal (Ni or Co), gray: carbon, red: oxygen, and white: hydrogen). (c) A representative hexagonal nanocrystal with the overlaid families of planes.

(HOPG),[33,34] and graphene.[35−37] While these materials benchmark performance for chemical detection in contemporary analyte−interferent systems, their lack of tunability from de novo synthesis and requirement for chemical modification to achieve competitive performance restrict directed development toward specific analytical targets. Studies have shown that carbon surfaces with fewer natural defects (i.e., the basal plane of HOPG) provide suboptimal properties as electrochemical interfaces for electron transfer kinetics and catalytic activity toward surface-sensitive probes compared to defect-rich surfaces.[38,39] To overcome this issue, selectivity and, in some cases, the sensitivity of these systems toward specific analytes can be greatly improved by postsynthetic modification using procedures that create functionalized or hybrid materials with improved sensing performance.[40−46] When compared with the bottom-up fabrication of functional materials, postsynthetic modification requires additional preparation steps, lacks chemical precision and atom economy, and is limited by available techniques.[47−49] A valuable complementary addition to working electrode technology would be a material system that can offer access to atomically precise electrochemical surfaces, the ability to install electrocatalytic subunits directly into the electrode material with chemical precision, seamless integration into devices, and a high degree of tunability in structure and morphology, while also conforming to the requirements of electrochemical applications (e.g., high conductivity and electrochemical stability). Obtaining these design features via a bottom-up synthetic procedure would produce a material with superior adaptability to a wide range of analytical systems.

Conductive 2D metal−organic frameworks[50,51] (MOFs) are promising functional materials for electroanalytical applications because they are readily prepared using highly tunable bottom-up methods, have a high surface area, and can be used to transduce chemical interactions into electrical signals.[52−54] Additionally, MOFs based on 2,3,6,7,10,11-hexahydroxytriphenylene (HHTP) are advantageous due to the fully conjugated nature of the HHTP ligand, which installs a rigidly extended π-framework, providing good conductivity and driving the self-assembly of 2D sheets into nanoscale crystalline solids.[55−60] The self-assembly of 2D sheets into layered crystallites creates three distinct surfaces: (1) edge facets rich in sheet termination sites within the crystallographic family of planes {100} (Figure 1A), (2) a basal plane that is rich in sp^2 carbons, axially

exposed metal ions, and cofacially aligned pores belonging to the crystallographic family of planes {001} (Figure 1B), and (3) interior pore volume with surfaces consisting of heteroatom lone-pairs and aromatic protons projected inwardly into the pore volume.

Each of the three chemically distinct surfaces of 2D layered conductive MOFs can provide a distinct set of interactions with their chemical environment, potentially allowing tailored degrees of control over electrochemical properties. While we[53] and others[61−64] have demonstrated that this general class of framework materials are capable of electrochemical detection and differentiation of biologically relevant organic analytes (BRO) such as dopamine (DA), uric acid (UA), ascorbic acid (AA), glucose, and serotonin (5-HT) at nM−μM concentrations, little is known about how morphology, dimensionality, and orientation of MOF nanocrystals impact the liquid-phase electroanalytical capabilities of these materials and how tuning these structural properties can be utilized to improve electroanalytical performance in multianalyte biologically relevant systems. This limitation restricts progress in the molecular design of conductive MOFs for targeted electroanalytical applications and prevents a fundamental understanding of emergent structure−property relationships at the nanoscale.

Herein, we demonstrate that specific crystalline facets of stacked 2D MOFs can be employed to impart advantageous properties toward liquid-phase electrochemical detection and enable the differentiation of biologically relevant organic analytes in complex multianalyte systems. We characterize the surface of preferentially oriented MOF nanocrystals by a combination of spectroscopy and microscopy techniques (e.g., XPS, SEM, PXRD), to determine structural properties, and electrochemical and computational methods to elucidate functional properties. We utilize well-known electrochemical probes that exhibit surface-sensitive and surface-insensitive properties to demonstrate that electrochemically relevant interfaces of epitaxially oriented MOF nanocrystals are dominated by three main morphologically tunable aspects arising from the anisotropy inherent in the structure of these framework materials: (1) hierarchical surface area as a geometrically complex diffusion interface; (2) Coulombic interactions between the surface charges on the MOF and charged analyte species in solution; and (3) intermolecular interactions between probes and the basal plane versus edge

sites. We demonstrate how these three aspects of the MOF materials determine their range of function, sensitivity toward targeted analytes, and selective response.

To investigate these aspects and their resulting properties, we examine the electroanalytical and electrocatalytic capabilities of $M_3(HHTP)_2$ (M = Co, Ni) under three degrees of structural control. First, we demonstrate that MOFs provide advantages compared to a glassy carbon electrode (GCE), such as increased sensitivity toward select neurochemical BROs (i.e., DA, 5-HT, and UA). Second, preferentially orienting the MOFs to expose either their basal plane having {001} facets or edge sites having {100} facets allows control over their exposed surface chemistry and characteristics of electron transfer to analytes in solution. For diffusion-controlled inorganic probes, we show that electrochemically active surfaces of $M_3(HHTP)_2$ can be preferentially organized through self-assembly into interfaces that promote or inhibit heterogeneous electron transfer rates (HETRs) ($k^0_{\{100\}}$ of $K_3Fe(CN)_6$: ~4.8 × 10^{-5} cm/s, $k^0_{\{001\}}$: not observed). Third, this morphological tunability proved a successful method of enhancing the detection of desired analytes and diminishing the influence of unwanted interferents in electroanalytical systems. Specifically, we show that epitaxially grown interfaces of {001} $Ni_3(HHTP)_2$ can enhance sensing characteristics compared with bulk synthesized material toward biologically relevant organic analytes, such as DA (LOD = 9.9 nM), in the presence of challenging interferents such as 3,4-dihydroxyphenylacetic acid (DOPAC) (LOD of DA = 381 nM in 50 μM DOPAC, 48 nM in 5 μM DOPAC) and in simulated cerebrospinal fluid containing elevated levels of soluble protein, uric acid, and glucose. The LOD for DA under these conditions was 214 ± 48 nM. Finally, we used Langmuir isotherm studies in conjunction with all-atom molecular dynamics (MD) simulations to demonstrate that the analytical differences stemming from structural–chemical tunability come from the specific adsorption motifs analytes experience on each electrode interface described by parameters, such as adsorption strength ($\Delta G°$) and surface coverage (Γ_S). The identification of interfaces that dominate electrocatalytic activity, the demonstration of rationally designed surfaces for the enhancement of chemical and electrochemical transformations, and the detailed investigation into the origins of the enhancement provide valuable contributions to the study and design of anisotropic stacked 2D nanomaterials for electrochemical applications.

EXPERIMENTAL DESIGN

Choice of MOFs. In this study, we chose two isostructural MOFs as representative materials for conductive 2D stacked framework systems. The two MOFs, $Co_3(HHTP)_2$ and $Ni_3(HHTP)_2$, were desirable as materials of inquiry because $Ni_3(HHTP)_2$ has been previously reported for its electrochemical sensing capabilities,[53] while also being isostructural with $Co_3(HHTP)_2$, which has a reported crystal structure.[55,57] Together, these materials allow molecular contributions to be studied alongside epitaxially controlled properties. Both MOFs possess at least three important attributes as model systems for 2D conductive materials applied to electrochemical sensing. First, they exhibit limited redox activity in aqueous biologically relevant buffer systems, such as phosphate-buffered saline (PBS) and KCl, and therefore show promise for detecting electroactive analytes in the −0.7–0.7 V (vs Ag/AgCl) potential range.[53] Second, they have demonstrated abilities

to detect a broad range of analytes in aqueous solutions $[Ni_3(HHTP)_2]$[53,64] and the gas phase $[Ni_3(HHTP)_2$ and $Co_3(HHTP)_2]$[65,66] using voltammetric and amperometric techniques, respectively. Third, they are readily accessible as nanocrystals with tunable (e.g., sheet- or rod-like) morphologies and are amenable to epitaxially controlled device-integration strategies.[57,60,67]

Despite these reported properties, little is known about how the anisotropy of common morphologies of 2D MOFs (nanorods) influences their electrocatalytic and electroanalytical properties. We hypothesized that the two distinct surfaces of stacked 2D materials could have dramatically different properties in electroanalysis and decided to investigate their individual properties through morphological control. In addition to a thorough examination of all MOF materials using a range of electrochemical methods, we also singled out $Ni_3(HHTP)_2$ {001} and $Ni_3(HHTP)_2$ {100} for detailed investigations using differential pulse voltammetry and Langmuir adsorption isotherm studies because they showed the most promising analytical properties. To aid in these studies we also subjected the two Ni-based MOF morphologies to additional characterization techniques. Area density of thin films is an important feature underpinning their electrochemical sensitivity. In this work, we chose the thickness of MOF films having exposed {001} planes because they were the thinnest cohesive films we could obtain by our interfacial synthesis method without compromising structural integrity or quality (i.e., fidelity of crystallite orientation, continuity of the film, and long-range coverage). Additionally, when investigating individual facets, we chose to use the thinnest possible film to promote a strongly leveraged ratio of exposed {100} or {001} facets. Thicker films (larger crystallites along the *c*-axis) would lead to a greater portion of {100} character in the films, which was undesirable for this study of specific families of planes.

Choice of Electrochemical Probes. The electrochemical activity of distinct interfaces was determined by quantifying the redox properties of inorganic and biologically relevant organic analyte probes. The redox activity of probes at interfaces can be characterized as surface-sensitive, surface-insensitive, or adsorption-controlled depending on their alacrity for uncatalyzed redox transformations.[68,69] Surface-insensitive probes typically display fast redox kinetics independent of the interface involved in the electron transfer process. Surface-sensitive probes display fast kinetics at interfaces that are conducive to electron transfer while displaying slow kinetics at interfaces that hinder electron transfer.[70] Adsorption-controlled probes require the formation of intermolecular interactions (e.g., hydrogen bonding, dispersion) with a surface in order to facilitate redox transformations.

Inorganic Probes. In this study, we chose the following three inorganic probes: $K_3Fe(CN)_6$, $Ru(NH_3)_6Cl_3$, and K_4IrCl_6 (all inorganic probes were used in CV experiments at 1 mM). This set of probes is widely used in the electrochemical literature and provides a strong foundation with which to investigate the electrochemical properties of electrode materials.[24] In contrast to BRO probes, they can be selected to represent a range of surface sensitivities and are less prone to side reactions and fouling of electrode surfaces. Fast redox kinetics observed for $K_3Fe(CN)_6$ indicate that a surface possesses functionalities and a density of states that are beneficial for facilitating electrochemical processes. The inorganic probes $Ru(NH_3)_6Cl_3$ and K_4IrCl_6 are well-known

surface-insensitive redox probes at carbon-rich surfaces such as graphene[36,71] and carbon nanotubes.[72] Their insensitivity to surface functionalization can be used as a control to confirm that surfaces with slow electron transfer kinetics observed for $K_3Fe(CN)_6$ exhibit reduced reactivity based on interactions between the probe and electrode, not reduced conductivity of the functionalizing MOF layer compared to GCE or limitations in function imposed by integration or deposition of materials on an electrode. Initially we were concerned that the small amount of {100} facet still present at the edges of {001} oriented films could contribute to the electrochemical response and obscure deconvolution of the electrochemical characteristics of each interface ({100} versus {001}) separately. Using a combination of surface-insensitive and surface-sensitive probes allowed us to distinguish between surface chemistries at each interface and determine the role, if any, of the {100} edges present in the {001} films.

BRO Probes. Accurate electrochemical detection and monitoring of electroactive BRO probes, such as DA, DOPAC, UA, and AA, have become crucial for the diagnosis and treatment of many diseases (Figure S21).[73,74] For example, DA and DOPAC play important roles in the molecular pathogenesis of stress reactions, cardiovascular diseases, hypertension, Parkinson's disease, depression, schizophrenia, and more.[74−77] Metabolites, such as UA,[78] and cofactors, such as AA,[79] both impact physiological function and act as interferents to the detection of other BROs.[80] Neurological pathologies can be especially difficult to diagnose chemically, and the direct, continuous, and minimally invasive detection of chemical biomarkers implicated in neurological disorders would provide better defined diagnostic protocols as well as the potential for improved understanding of the mechanisms of these diseases.[81,82] We chose to characterize our MOF electrode materials against the probes DA (10 μM), DOPAC (100 μM), 5-HT (10 μM), UA (100 μM), and AA (100 μM).

The electrochemical properties of these probes have been well studied on a wide array of surfaces such as graphene,[83] MOFs,[53] gold,[84] and multicomponent coatings.[40,85] Their interaction with electrodes is highly dependent on their ionicity, the charge of the electrode, and surface functionality capable of facilitating their electrochemical transformation.[84,86,87] The oxidation and reduction of DA, DOPAC, and 5-HT involve two-electron, two-proton processes (Figure S21).[27,84,88−90] Exploring these probes can allow for an improved understanding of structure−property relationships and elucidate the importance of controlled epitaxial orientation on the kinetic capabilities of these MOF-based electrodes.

Choice of Electrochemical Methods. For this work a three-electrode configuration consisting of a working, a reference, and a counter electrode was used to allow accurate measurements of current and minimize the influence of capacitive double-layer effects in voltammetric measurement regimes.

Choice of Electrodes. Glassy carbon was chosen for the working electrode for its moderate kinetics and chemical inertness. MOF materials were mounted on the GCE to provide a low-resistance, water-stable, chemically inert method of applying a working potential from the potentiostat to the materials of interest. The counter electrode was chosen to be platinum for its ability to enable high current density and inertness over a wide potential range. An AgCl-coated Ag wire in 1 M KCl was chosen as the reference electrode because of its well-known stability, reproducibility, compatibility with aqueous chemistry, and convenient reduction potential versus the standard hydrogen electrode (Ag/AgCl: +0.235 V vs SHE).

Choice of Electrolyte. The supporting electrolytes chosen for this study were either 0.1 M KCl or 0.1 M PBS (pH = 7.4). The unbuffered saline solution, 0.1 M KCl, was chosen for its sufficient conductivity (reducing the series resistance of the electrochemical cell) as well as the inert nature of the K^+ and Cl^- components. KCl electrolyte was primarily used in experiments having no biologically relevant components. The electrolyte composed of PBS (0.1 M, pH = 7.4) was chosen to replicate conditions typically associated with electrochemical sensing of BROs. The drawback of PBS is that the phosphate anions have low solubility with divalent transition metals (K_{sp} ~ $10^{-32}−10^{-37}$).[91,92] This low K_{sp} indicates that PO_4^{2-} could be capable of leaching metals from MOFs or capping exposed metal sites on MOF surfaces. To provide context for in vivo sensing applications, we also examined the ability of the nanomaterial $Ni_3(HHTP)_2$ to detect DA in a mimic of cerebrospinal fluid containing the following: 42 μM UA, 4 mM glucose, and 0.5% bovine serum albumin (BSA) in PBS. The judicious usage of the three electrolyte solutions, having distinct properties, ensured accurate characterization under various conditions such as biological relevance and the fidelity of pristine MOF surfaces.

Choice of Electrochemical Techniques. Cyclic voltammetry was the primary method of investigating materials mounted on GCE. Cyclic voltammetry was used because it allows a wealth of information to be gathered about electrode materials, electrode−electrolyte interfaces, and the kinetics and thermodynamics of electrochemical transformations of probe analytes at electrode surfaces. Voltammetric data were collected over scan rates starting at 1000 mV/s down to 5 mV/s. For inorganic probes, the peak separation between oxidation and reduction waves was used to determine the HETR constant as k^0 for electrode−probe systems. Because reaction systems at electrodes can be reversible, quasi-reversible, or irreversible, for a variety of chemical, kinetic, and thermodynamic reasons, only reactions exhibiting reversible or quasi-reversible voltammograms were characterized to determine k^0. Practical application of the Nicholson−Shain[93] and Klinger−Kochi[94] methods was accomplished by applying the equation describing an extended working curve developed by Magno and co-workers (eq 1).[95]

$$\Psi = (-0.6288 + 0.0021X)/(1 - 0.017X) \tag{1}$$

For systems that exhibited irreversible electron transfer characteristics or irreversible chemical transformations (identified by peak separations > 300 mV, or where kinetic parameters were no longer applicable, or irreversible CVs), HETR constants were not calculated. We typically encountered these cases for the BROs. Similarly, in electrochemical systems where the probe was under an adsorption regime rather than diffusion control, the HETR constants were not calculated. An experimental determination of the diffusion coefficient for analytes with each electrode system was needed to determine k^0. This value was obtained by plotting the peak potential versus the square root of the scan rate to generate Randles−Ševčík plots (R−S plots) for the fully reversible case.

To examine electron transfer rates, redox probes were studied across a potential window of −0.7 to 0.7 V vs Ag/AgCl. This potential window was chosen as it encompasses the oxidation and reduction potentials of the analytes examined.
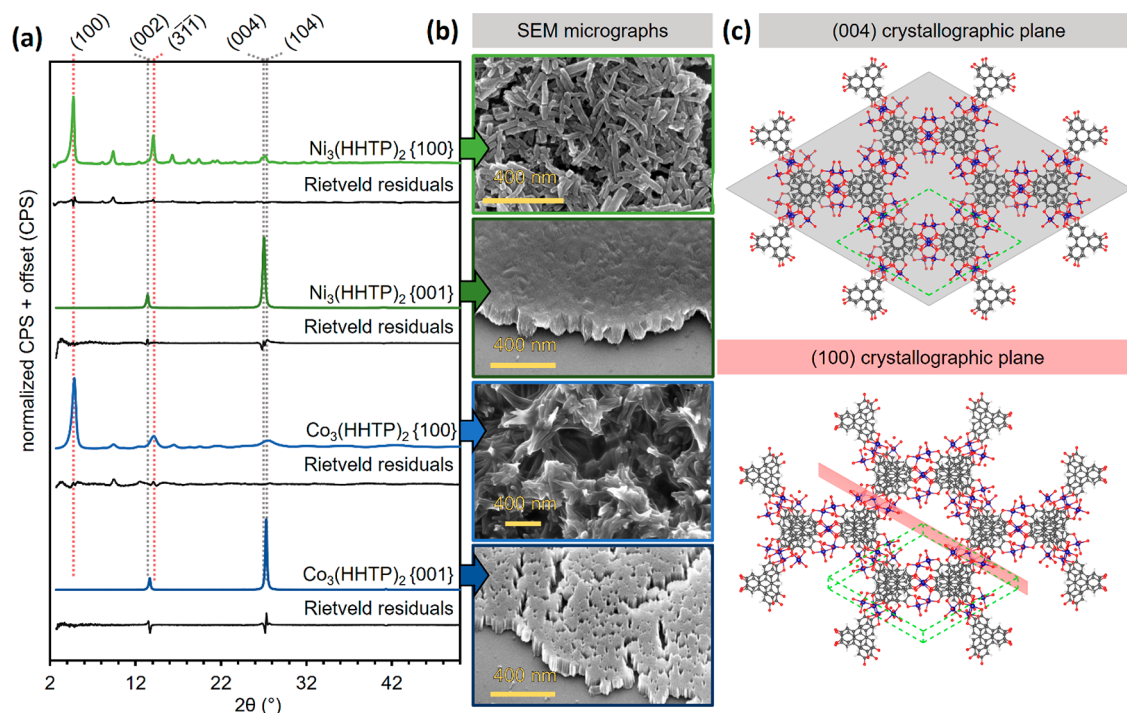
Figure 2. (a) PXRD diffractograms of the {100} and {001} preferential orientations of $Ni_3(HHTP)_2$ and $Co_3(HHTP)_2$. The residuals from the Rietveld refinement process are shown below each PXRD trace. Characteristic diffraction lines and their corresponding (*hkl*) planes depicted in gray and red correspond to the basal plane and edge plane crystallographic planes, respectively. Corresponding SEM images of the materials characterized by PXRD (b) showing the orientation of materials on the substrate. (c) The crystallographic planes corresponding to the strongest diffractions observed in the {001} (top) and {100} (bottom) materials. The diffraction plane is shown in either gray or red, and the unit cell is shown in green. Atoms are depicted as gray, carbon; red, oxygen; blue, metal (Ni or Co); white, hydrogen.

Oxidation and reduction of target analytes occur at specific potentials determined by factors related to the working electrode (electrode geometry, overpotential, electron transfer rate, scan rate, and diffusion coefficient) and the electrochemical system (nature of target probe). For investigations using inorganic probes, 0.1 M KCl was used as the electrolyte. When examining BROs, 0.1 M PBS (pH = 7.4) was used as the electrolyte.

Since the materials used in this study were both nanostructured and highly porous, the addition of material deposited on the GCE was anticipated to enhance the electrochemical surface area (ECSA) of the working electrode compared to unmodified GCE. The ECSA was determined by monitoring current density in non-Faradaic regions. Current densities monitored over multiple scan rates provided the double-layer capacitance (C_{dl}), which could then be compared to unmodified GCE. The roughness factor obtained was then used to scale the surface area of the working electrode to account for the increased surface area when functionalized with MOF nanomaterials.

Electrochemically derived Langmuir isotherm studies can be used to investigate how analytes adsorb to electrode surfaces. For analytes such as DA that adsorb to electrode surfaces during oxidation/reduction, these isotherms provide information such as the density of host sites on the electrode material and the thermodynamics of adsorption.[45] We used Langmuir adsorption isotherms to quantify MOF–analyte interactions to gain deeper insight into the material properties governing analytical sensitivity and selectivity. The Langmuir model provides information about the ensemble-level interactions occurring at the morphologically tuned surfaces of

$Ni_3(HHTP)_2$ {100} and $Ni_3(HHTP)_2$ {001} (Supporting Information Section XVII).

RESULTS AND DISCUSSION

Morphological Control of Oriented Electrochemically Accessible Crystal Facets. $Ni_3(HHTP)_2$ and $Co_3(HHTP)_2$ are isostructural frameworks. They possess similar packing structures of alternating layers and honeycomb lattices.[55,57] In this study, we achieved epitaxially oriented surfaces of MOF nanocrystals through morphological control of MOF crystallites under hydrothermal synthetic conditions.[55] Previously, both step-by-step epitaxial methods and solid–liquid interface methods have been applied to achieve enhanced *c*-axis orientation of nanocrystalline MOFs.[57,96] Preceding studies have indicated that the thickness of the films in addition to the composition of the films is an important tunable feature.[67] Herein, we synthesized rod-like and sheet-like assemblies of nanocrystals under hydrothermal and interfacial reaction conditions and achieved deposition on GCE either through drop-casting or Langmuir–Blodgett techniques (Supporting Information Section II). Rod-shaped crystallites were produced using previously reported hydrothermal conditions and drop-cast directly from the reaction solution either onto GCE for the fabrication of working electrodes or onto the surface of a glassy carbon substrate (Figures S5, S17, S18) or SI wafers for physical analysis (Supporting Information Sections II–VI). Sheet-like crystallites were grown at the interface between an anoxic aqueous solution and ambient air (Figure S5) and were transferred onto surfaces (GCE or Si) using the Langmuir–Blodgett technique.[55] The similar manner in which samples
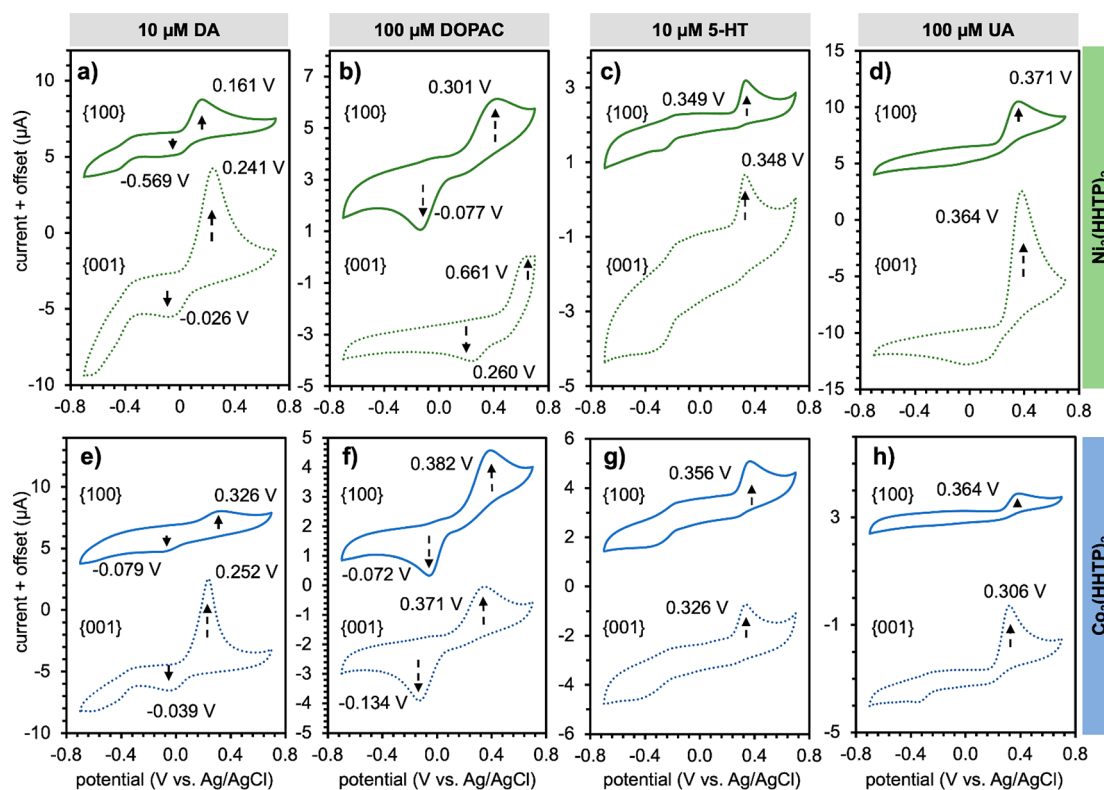
Figure 3. Cyclic voltammograms of (a−d) Ni$_3$(HHTP)$_2$ {100} and {001} interfaces with DA, DOPAC, 5-HT, and UA. (e−h) Cyclic voltammograms of Co$_3$(HHTP)$_2$ {100} and {001} interfaces with 10 μM DA, 100 μM DOPAC, 10 μM 5-HT, and 100 μM UA. All voltammograms were recorded in 0.1 M PBS at a pH of 7.4. A scan rate of 50 mV/s was used to obtain all traces across a scan window of −0.7−0.7 V (vs Ag/AgCl). Traces have been offset vertically for clarity.

were prepared across physical characterization procedures and electrochemical experiments allowed the morphology determined by SEM to be compared with observations of crystallinity and epitaxial orientation obtained by PXRD and implicated in results of electrochemical experiments.

SEM imaging of the silicon-mounted samples revealed that the materials prepared by the Langmuir−Blodgett method consisted of highly aligned bundles of crystallites with their hexagonal faces parallel to the silicon plate (Figure 2b, Figures S2, S4, S5). Hydrothermally obtained materials revealed a rod-like crystalline habit with a random distribution of orientations relative to the plane of the silicon plate (Figures 2b, S1, S3). SEM also revealed that the nanorod materials were distributed evenly across the surface as a film when deposited from a suspension.

We anticipated that the large sheet-like plane of the Ni$_3$(HHTP)$_2$ and Co$_3$(HHTP)$_2$ MOFs observed by SEM would be coplanar with the molecular basal plane corresponding to the Miller indices defined by the family of planes {001}, meaning the dominant exposed interface would be the basal plane (Figure 1). Similarly, we anticipated that the majority surface area of the hydrothermal synthesis was described by the set of Miller indices defined by the family of planes {100}, meaning that the majority of exposed surface area was terminal edge sites.

To confirm these premises, the crystallinity and preferential orientation of both morphologies were assessed by PXRD with Rietveld refinement. The highly oriented interfacially grown materials, characterized by powder X-ray diffraction (PXRD), exhibited a single strong diffraction peak at 27.5° 2θ that was calculated to arise from an intermolecular distance of 3.34 Å

(Figure 2a). By comparison with computational models and single-crystal structures of previously reported isostructural Co$_3$(HHTP)$_2$, we determined the Miller index of the corresponding diffraction plane to be (004) (Figure 2a,c).[55]

Rietveld refinement was used to confirm that the interfacially grown sheet-like films of both Co$_3$(HHTP)$_2$ and Ni$_3$(HHTP)$_2$ had a nearly quantitative alignment of the c-axis of the crystalline domains within the polycrystalline film aligned perpendicular to the PXRD substrate (Figure 2a, Supporting Information Section V). The orientation observed for the sheet-like film confirmed that interfaces observed by SEM were indeed the basal plane of the MOF (Figure 2b).

PXRD analysis of the rod-like hydrothermal nanomaterials of Co$_3$(HHTP)$_2$ and Ni$_3$(HHTP)$_2$ exhibited a prominent diffraction peak at 4.6° 2θ corresponding to an interatomic distance of 18.0 Å commensurate with the anticipated prominence of the (100) diffraction plane (Figure 2a,c). Rietveld refinement identified a slight preferential orientation of the nanorods having their c-axis parallel to the substrate. This result matched the observed orientation of nano-crystallites observed by SEM (Figure 2b, Supporting Information Section V).[55] In the future, additional studies with wide-angle X-ray scattering could aid in the determination of crystallite orientation in thin-film systems such as these. Having confirmed that the synthesized materials had interfaces with the anticipated orientations, we then examined the chemical composition of the crystalline facets by XPS analysis. Survey spectra of the four distinct materials showed similar features including elemental emission lines corresponding to O 1s and C 1s transitions as well as the corresponding metal for each MOF (Co or Ni) (Figures S15, S16). Additional

characterization using energy dispersive X-ray spectroscopy confirmed the presence of the expected elements as well as their even distribution throughout the materials (Figures S17, S18).

After confirming that the synthetic methods we developed and the material integration methods we used provided access to specific crystalline facets with good fidelity, we assessed the response of these two distinct orientations using electrochemical methods. Because we wanted to determine how the analytical properties of the materials changed on each facet, we chose to first study the electrochemical properties of these materials with redox-active inorganic probes.

The Electrochemical Response of the {100} Facet and the {001} Facet of MOFs toward Inorganic Probes. Analysis with inorganic probes served two primary purposes. First, we used these probes to identify electrochemically distinct properties specific to the {001} or {100} interfaces of $M_3(HHTP)_2$. Second, although the orientation of the materials appeared quantitative by SEM and PXRD, we were cognizant of the inextricable nature of the individual facets. That is, even in the sheet-like materials dominated by the surface chemistry of the {001} interface, edge sites were still present at the exposed columnar edges of the tightly packed and aligned rods. Additionally, preferred orientation of particles does not guarantee that electrolytes and analytes will access a particular facet over others. We investigated the electrochemical properties of each of the four distinct materials toward two types of inorganic redox-active agents, surface-sensitive ($K_3Fe(CN)_6$) and surface-insensitive probes ($Ru(NH_3)Cl_3$ and K_4IrCl_6).

Our initial experiments with surface-insensitive probes served as a control experiment for both morphologies. All four of the materials we examined using CV, including sheet-like ({001}) and rod-like ({100}) $Co_3(HHTP)_2$ and $Ni_3(HHTP)_2$, showed similar kinetics and peak currents for the surface-insensitive inorganic probes $Ru(NH_3)Cl_3$ (Figures 4a, S24, S32) and K_4IrCl_6 (Figures 4a, S26, S34). From these similar results, we were confident that both the {001} and {100} interfaces exhibited good contact with the underlying GCE, were conductive enough to allow electrochemical characterization and use in analytical applications, and that any differences we observed in further experimentation were indeed originating from differences within the materials rather than extrinsic experimental properties.

Next, we examined the MOFs using CV and the surface-sensitive $K_3Fe(CN)_6$. Here we observed dramatic differences in HETR k^0 between materials having predominantly {001} orientations (sheet-like morphologies) and {100} orientations (rod-like morphologies). While the {100} $M_3(HHTP)_2$ materials provided observable HETR k^0 values, albeit significantly slower than bare GCE, the {001} interface of $M_3(HHTP)_2$ showed no discernible ability to engage in redox transformations of the $[Fe(CN)_6]^{4-/3-}$ probe (Figures 4a, S25, S33). The dramatic differences in activity we observed for surface-sensitive probes but not for surface-insensitive probes confirmed that the morphologically obtained interfaces defined which facets were predominantly performing electrochemical transformations, specifically that the {100} surface area present in the oriented {001} films did not play a significant role in electrochemical experiments.

Our observations demonstrated that the reactivity of electrochemical surfaces can be tuned by controlling the morphology of the active material. We also demonstrated that
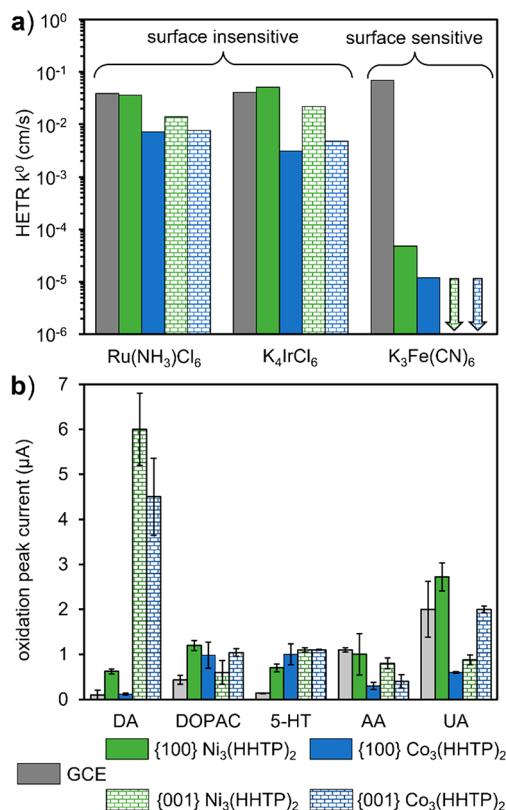
Figure 4. Summary of electrochemical properties of $Co_3(HHTP)_2$ and $Ni_3(HHTP)_2$ electrodes having {100} and {001} preferential orientation. For inorganic probes (a) the figure of merit is the heterogeneous electron transfer rate constant (HETR k^0) for surface-insensitive (i.e., $Ru(NH_3)_6Cl_6$ and K_4IrCl_8) and surface-sensitive (i.e., $K_3Fe(CN)_6$) probes. For biologically relevant organics (BRO) (b) the figure of merit in analytical applications is the observed peak current. This value is obtained from the oxidative wave of cyclic voltammograms. The data for inorganic probes were collected from solutions of 0.1 M KCl and an analyte concentration of 1 mM. For BROs, CVs were collected in a solution of 0.1 M PBS at a pH of 7.4. The analyte concentrations were 10 μM for DA and 5-HT and 100 μM for DOPAC, AA, and UA.

self-assembly of preferentially oriented surfaces provides control over the electron transfer processes across the electrode−electrolyte interface. We hypothesize that this tunability is a function of two primary factors. First, like HOPG and graphene, the basal plane of the MOFs is inherently slower in electron transfer processes compared to edge sites. This is a phenomenon commonly observed in 2D materials where defect sites, such as growing edges, vacancies, and dislocations in the crystalline lattice, are the locations that harbor the highest density of states (DOS).[97] Second, surface chemistry of the edge sites is more advantageous for catalyzing the surface-sensitive transformation of specific probes like $[Fe(CN)_6]^{4-/3-}$.[98] Features such as DOS and surface chemistry together provide a means of affecting the electroanalytic properties for inorganic analytes. Having characterized the intrinsic features of the materials and their electrochemical properties toward inorganic analytes, we next looked to examine BROs.

Application of Morphological Control for the Detection of Biologically Relevant Organic Analytes. To expand our understanding of morphologically controlled
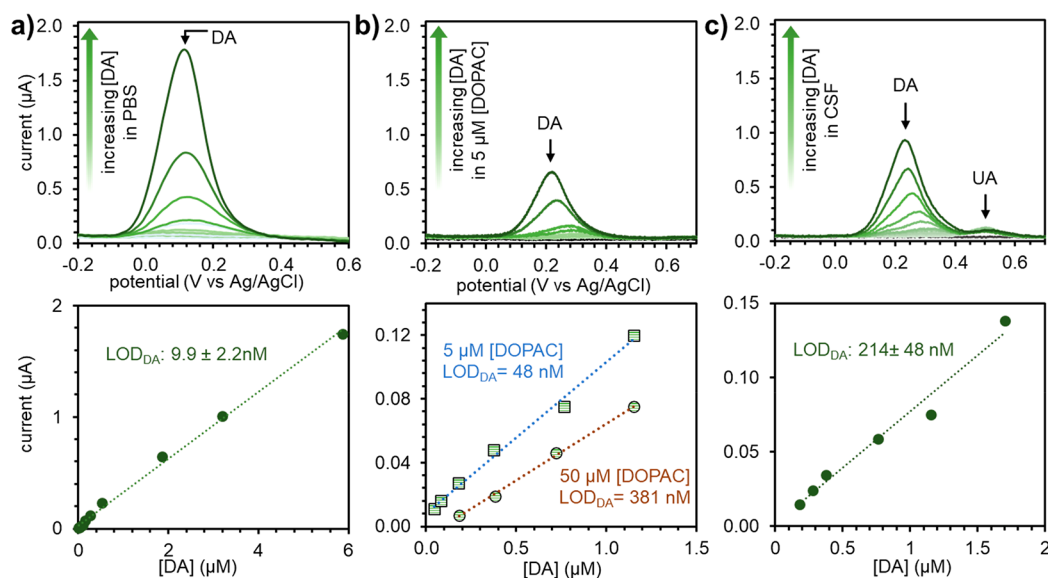
Figure 5. Sensitivity of Ni₃(HHTP)₂ {001} for the detection of DA using differential pulse adsorption stripping voltammetry (DPASV) in each distinct analytical solution. (a) DPASV traces of increasing [DA] in 0.1 M PBS. (b) DPASV of increasing [DA] in 0.1 PBS with overwhelming concentrations of 3,4-dihydroxyphenylacetic acid (DOPAC) including 5 μM DOPAC (blue traces) and 50 μM DOPAC (brown trace). (c) DPASV of DA in a solution of simulated cerebrospinal fluid (CSF) containing UA, glucose, and 0.5% bovine serum albumin. For all linear fits, $R^2 > 0.97$.

properties to BROs, we examined the electrochemical response of the {100} and {001} facets of M₃(HHTP)₂ to DA, DOPAC, 5-HT, UA, and AA. This selection of analytes was chosen because they present a range of oxidation potentials, surface sensitivities, and cationic and anionic species in solution. DA and 5-HT possess a positive charge when dissolved at pH 7.4, while DOPAC, UA, and AA are negatively charged at pH 7.4.

The Response of BROs at GCE. To benchmark analytical performance, we first measured the CVs of BROs on bare GCE. We generally observed weak peak currents (i_p) for all the BROs at GCE (Figures 4b, S23). We also observed lower overpotentials of analytes on GCE compared to the MOFs (Figures 3, S23). We anticipated that these differences could be explained by two phenomena. First, the strong peak currents observed for BROs at MOFs compared to the GCE are a product of the enhanced host—guest interactions (e.g., hydrogen bonding) and surface area provided by the MOF. Second, the higher overpotentials observed for BROs on MOFs compared to GCE could result from increased double-layer effects arising from created interfaces (GCE−MOF and MOF−electrolyte) in the electrochemical system. Another possibility is that the conductance of the polycrystalline MOFs is less than that of GCE, causing some uncompensated resistance to play a role.

Discussion of Epitaxially Controlled Facets of MOFs for Electroanalysis of BROs. The electrochemical response of analytes at MOF surfaces was measured for two MOFs (i.e., Co₃(HHTP)₂ and Ni₃(HHTP)₂) and five BROs (i.e., DA, DOPAC, 5-HT, AA, and UA, Figure 3, Supporting Information Section X, Section XII). Epitaxially controlling the integration of nanomaterials provided three broad levels of control. First, all MOFs in this study showed improved i_p over bare GCE for the BROs carrying a positive charge in solution (i.e., DA, 5-HT) and a worse response for probes carrying a negative charge (i.e., DOPAC, AA) despite these analytes being evaluated using a 10× concentration (Figure 4b). The improvement most likely stemmed from a combination of

properties such as complementary Coulombic interactions and differences in adsorption sites between GCE and MOF interfaces. Second, the {001} interface of both M₃(HHTP)₂ MOFs showed dramatically higher i_p for DA compared to the {100} interface (Figures 3, 4b). This difference between the i_p measured on the {001} versus {100} was not as pronounced for 5-HT and not observed for other BROs. Finally, Co₃(HHTP)₂ and Ni₃(HHTP)₂ (Figure 4b) showed similar electrochemical properties as one another for all the analytes, which suggested that metal identity (Co vs Ni) played a diminished role compared to morphology and exposed interface.

DOPAC is an important metabolite of L-DOPA and DA in physiological systems.[99] DA and DOPAC are often co-occurring but have significantly different physiological roles, necessitating their independent quantification. Our CV experiments showed that the MOFs had increased sensitivity toward DA and decreased sensitivity toward DOPAC compared to GCE, with DOPAC requiring 10× the concentration of DA to produce an equivalent observable response (Figures 3, 4b). We noted that the {001} facet of Ni₃(HHTP)₂ was more sensitive to DA, producing a 6× greater i_p compared to the {100} facet, while also shifting the oxidation peak of DOPAC toward higher potentials (Figure 3). We hypothesized that the electrochemical properties of the {001} facet of Ni₃(HHTP)₂ could be used to produce a selective electrochemical interface for the detection of DA.

The Sensing Performance of {100} and {001} Facets of Ni₃(HHTP)₂. To test this hypothesis, we used differential pulse adsorption stripping voltammetry (DPASV) to determine the LOD of DA in three different electrolyte formulations, including a 0.1 PBS electrolyte, a 0.1 M PBS solution containing high concentrations of the interferent DOPAC, and a simulated cerebral spinal fluid (CSF) containing 0.1 M PBS, 0.5% bovine serum albumin (BSA), 1 mM glucose, and 7 μM UA. In the simplest electrolyte solution, 0.1 M PBS, we found an LOD for DA of 9.9 ± 2 nM
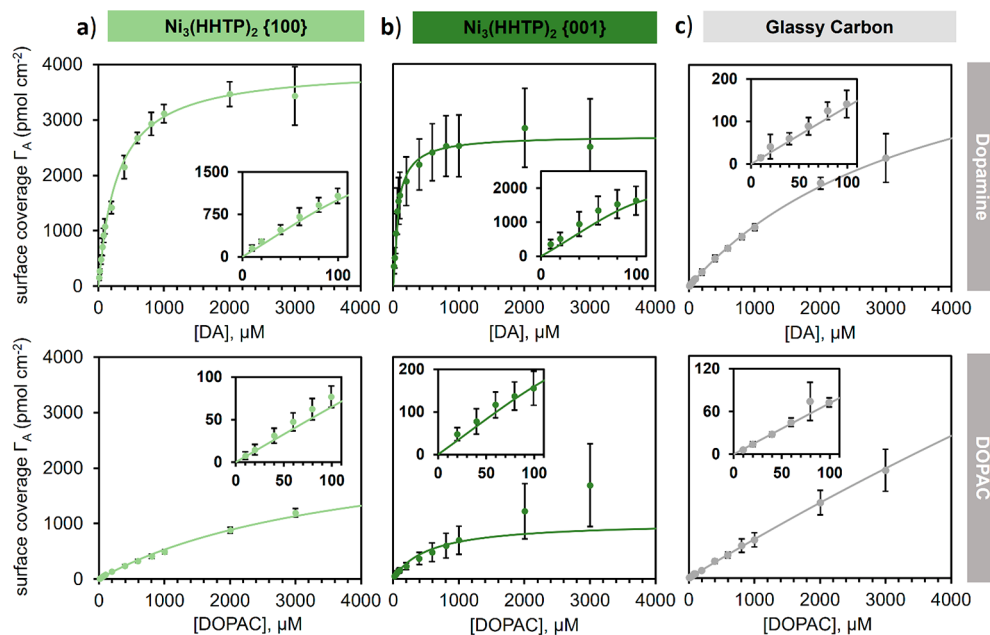
Figure 6. Langmuir isotherms presented as surface coverage (Γ_A) versus concentration [analyte] for dopamine (DA, top) and 3,4-dihydroxyphenylacetic acid (DOPAC, bottom), for electrodes composed of (a) $Ni_3(HHTP)_2$ {100}, (b) $Ni_3(HHTP)_2$ {001}, and (c) glassy carbon. Insets are included for each plot corresponding to surface coverages at low concentrations of analyte. Surface coverage at each concentration was calculated from peak current from the oxidative wave of a cyclic voltammogram (CV). CVs were performed at 50 mV/s in a solution of 0.1 M phosphate-buffered solution at a pH of 7.4.

([Figure 5](#)a, [Figure S43](#)). Next, we repeated the DPASV experiment with comparatively high concentrations of DOPAC. The first test measured a limit of detection of 381 nM for DA in a solution containing 50 μM DOPAC ([Figures 5b, S44](#)). When the concentration of DOPAC was reduced to 5 μM, the LOD of DA was measured to be 48 nM ([Figures 5b, S44](#)). Finally, in simulated CSF we measured a LOD for DA of 241 $\pm$ 48 nM with good separation between the oxidative waves of UA and DA and no observed interference from glucose ([Figures 5c, S45](#)).

This series of analytical experiments demonstrated three features of the MOFs. First, the inherent sensitivity of the {001} interface to DA allowed nM detection limits in biologically relevant PBS solutions. Second, we showed that the interface of 2D MOFs could be used to strategically modulate the response to analytes and interferents in analytical systems to select against interferents such as DOPAC, UA, and glucose. Third, the electrode system was able to perform in complex analytical environments such as those containing high concentrations of soluble protein (BSA). Full experimental data sets and concentration ranges can be found in the Supporting Information ([Sections XIV–XVI](#)).

Adsorption of DA and DOPAC on $Ni_3(HHTP)_2$. Electrochemical oxidation of DA and DOPAC requires adsorption of the analytes to electrode substrates. In our experiments, we observed that the oxidation of DA was largely irreversible at the scan rates (<1 V/s) and concentrations (10–100 μM) we investigated ([Figure 3](#)). We were therefore interested in determining how adsorption properties differed at each interface of the MOFs and if those adsorption parameters were underpinning the observed differences in analytical sensitivity and selectivity between the {001} and {100} interfaces of $M_3(HHTP)_2$. Because $Ni_3(HHTP)_2$ was the material we chose to advance toward analytical experiments and showed exceptional sensing characteristics, it was also the

material we decided to examine in our Langmuir isotherm studies. To characterize the interactions between DA and DOPAC with the two interfaces of $Ni_3(HHTP)_2$, we used both experimentally obtained adsorption parameters from Langmuir adsorption isotherms as well as MD simulations to elucidate adsorption motifs in MOF–analyte interactions.

The Langmuir model assumes that a fixed number of heterogeneous host sites are available for adsorption, adsorption sites are energetically equivalent, and that exactly one analyte adsorbs at each host site.[100] While these assumptions limit the ability to differentiate between multiple distinct adsorption interactions that may be occurring on the anisotropic MOF surface, the Langmuir model can still provide information on the ensemble of interactions occurring at the morphologically tuned surfaces of $Ni_3(HHTP)_2$ {001} and $Ni_3(HHTP)_2$ {100} ([Supporting Information Section XVII](#)). We used the oxidative peak current maxima derived from cyclic voltammograms to calculate the electrode surface coverage (Γ_A) at concentrations spanning the range [DA] = 10 μM–3 mM using [eq S1](#).[101] Plotting Γ_A for each analyte concentration provided a curve that was fit with Langmuir's isotherm equation ([eq S2](#)), which allowed us to extract the saturation surface coverage, Γ_S, and the thermodynamic equilibrium constant, β, that describe the ensemble of adsorption interactions.[101] These values were then used to calculate the Gibbs free energy of adsorption, $\Delta G°$, using [eq S3](#).[101]

The isotherms for $Ni_3(HHTP)_2$ {100}, $Ni_3(HHTP)_2$ {001}, and GCE adsorbing the analyte DA or DOPAC are shown in [Figure 6](#); 3–6 replicates of each experiment were conducted. The curves were fit using a weighted least-squares regression model, meaning that the points with the least uncertainty had the greatest impact on the fitted curve ([Supporting Information Section XVII](#)).

By qualitatively comparing the isotherms based on the shape of the curve and magnitude of Γ_A values, we identified that

$Ni_3(HHTP)_2$ materials behave differently than GCE in adsorbing DA versus DOPAC, indicated by their measured Γ_S, β, and $\Delta G°$ values. The Γ_S, β, and $\Delta G°$ derived from the isotherm plots are compared in the Supporting Information Table S2.

Interpretation of Langmuir Isotherm Studies. The isotherm studies involving the adsorption of DA and DOPAC to electrode surfaces composed of $Ni_3(HHTP)_2$ {100}, {001}, and GCE yielded the parameters Γ_S, β, and $\Delta G°$ visualized in Figure 7a−c, respectively. We found key
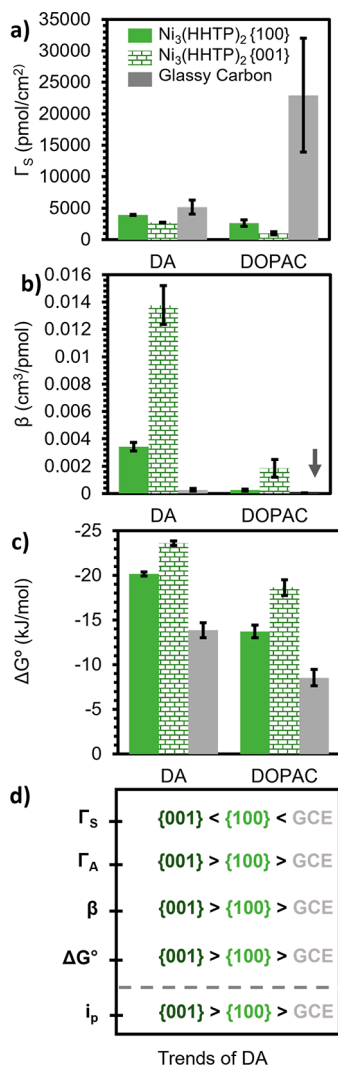
Figure 7. Summary of data obtained from Langmuir isotherm studies for the adsorption of the analytes DA and DOPAC to electrodes composed of $Ni_3(HHTP)_2$ {100} and {001}. (a) Surface coverage Γ_S, (b) thermodynamic equilibrium constant β, (c) Gibb's free energy of adsorption $\Delta G°$, and (d) comparison of the trends in the adsorption of DA compared to the electrochemical response for DA (peak current and Γ_A reported for [DA]: 10 μM) for the three electrode materials.

trends for all three of these adsorption metrics that held true for both DA and DOPAC. First, we found that $Ni_3(HHTP)_2$ {001} had the lowest saturation surface coverage (Γ_S) and GCE had the highest saturation surface coverage for both analytes (Figure 7a, Table S2). Second, the equilibrium constant of adsorption (β) for DA and DOPAC was dramatically higher for $Ni_3(HHTP)_2$ {001} compared to

$Ni_3(HHTP)_2$ {100} and was lowest for GCE. Third, we found that the adsorption strength ($\Delta G°$) of the analytes was greater (more negative) on $Ni_3(HHTP)_2$ interfaces compared to GCE and was largest on the $Ni_3(HHTP)_2$ {001} interface (Figure 7c, Table S2). These three trends were then compared to the i_p values of DA at 10 μM measured by CV (Figure 7d, Table S2). We found that greater values of β and more favorable values of $\Delta G°$ (more negative $\Delta G°$) followed the trend of i_p for DA ({001} > {100} > GCE).

Γ_A (pmol cm^{-2}) indicates the density of occupied host sites at a particular concentration, while Γ_S (pmol cm^{-2}) indicates the maximum density of available host sites for an electrode material. Higher Γ_A values contribute directly to higher peak currents in voltammetric analysis.[45] For trends in saturation surface coverage (Γ_S) we observed separate regimes at high and low concentrations of DA. At low concentrations ([DA] < 100 μM, Figure S47), we observed that Γ_S trended against Γ_A. This relationship indicated that at low concentrations the $Ni_3(HHTP)_2$ {001} was a more sensitive electrode interface for detecting DA. At concentrations above this regime ([DA] > 100 μM, Figure S47) we observed a correlation between Γ_S and Γ_A for DA, which suggested that the higher saturation coverage was dominating the response. The relationship between β (cm^3 pmol^{-1}) and i_p was useful in understanding the difference observed between Γ_S and Γ_A. At subsaturating concentrations the magnitude of β describes the portion of active sites occupied by analyte. For voltammetric analyte detection in the nM range, β becomes an important descriptor of how many DA are adsorbed (i.e., what fraction of adsorption sites are occupied) and can be oxidized as a function of solution-phase concentration. The magnitude of β stems from the favorability of analyte−material interactions ($\Delta G°$), meaning that the exergonicity of the adsorption governs the surface coverage at subsaturating concentrations.[101] In summary, we found that at low concentrations ([DA] < 100 μM, Figure S47) the greater β exhibited by the {001} interface produced a higher surface coverage, Γ_A, and thus a stronger electrochemical response. At high concentrations ([DA] > 100 μM) the greater number of host sites, Γ_S, on the {100} surface was the most important factor for designing a sensitive electrode interface. To understand why the {001} interface of $Ni_3(HHTP)_2$ had a more favorable β and $\Delta G°$ compared to the {100} interface, we conducted all-atom MD simulations to understand material features important to favorable analyte adsorption.

MD Simulations of Interactions between $M_3(HHTP)_2$ MOFs and Neurochemicals. The electrochemical methods used in this study were limited in their ability to determine specific features of adsorption between analytes and the MOF interfaces. To inform our isotherm findings, we aimed to identify chemical features responsible for the differences in surface coverage and adsorption strength. To probe these aspects of analyte adsorption, we conducted MD simulations of systems comprising DA or DOPAC with each MOF. Each system was created by placing one type of MOF ($Co_3(HHTP)_2$ or $Ni_3(HHTP)_2$) at the center of the simulation domain (Figure S48), then adding 27 molecules of a given analyte of interest (DA or DOPAC) around the MOF (Figure S49). Each system was then solvated with TIP3P water molecules and equilibrated for 100 ps at 293 K and 1 atm. Following equilibration, MD simulations were performed in the NPT ensemble on each system for 20 ns with a time step of 2 fs using the DL_POLY_4 package.[102]

The results from all-atom MD simulations (Figures 8, S51) provided a set of visualized interactions between DOPAC and
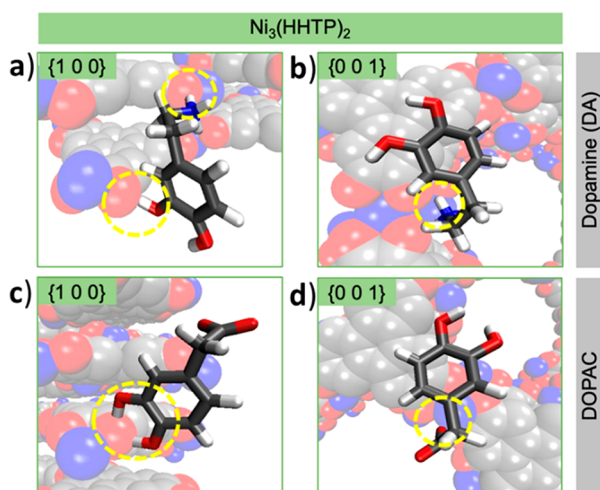
Figure 8. Interactions between analytes and $Ni_3(HHTP)_2$ observed during MD simulations. Structures of the MOFs are represented by spheres (blue = Ni, gold = Co, red = O, gray = C, protons and aqua ligands were removed for clarity), and analytes are represented by stick structures. Interactions of DA with $Ni_3(HHTP)_2$ at the (a) {100} and (b) {001} interfaces. The adsorption of DOPAC at the (c) {100} and (d) {001} interface of $Ni_3(HHTP)_2$.

DA at each MOF interface (Tables S3−S6). The sampling of adsorbed structures we obtained provided a molecular-scale understanding of analyte interactions at each interface. As expected, interactions between the catecholate-based analytes and the {100} facet of $M_3(HHTP)_2$ were dominated by hydrogen-bonding interactions with terminal aqua ligands, as well as heteroatoms of the HHTP ligands. In contrast, the {001} facet of $M_3(HHTP)_2$ was able to host hydrogen-bonding interactions as well as hydrophobic $\pi-\pi$ interactions. These two observations, increased areal density of host sites at the {100} interface and mixed bonding (H-bonding and π-bonding) types at the {001} interface, were then used to further interpret the results from our Langmuir isotherm adsorption studies.

Insight into Electrochemical Properties from Electrochemical Experimentation and MD Simulations. Adsorption parameters obtained from Langmuir isotherm studies and results obtained from MD simulations pointed to the role of surface coverage and adsorption strength in determining the analytical performance of $Ni_3(HHTP)_2$ electrodes. Surface coverage (Γ_S), which we experimentally identified as trending inversely with electroanalytical sensitivity, was higher for DA on {100} than {001} and appeared to originate from the dense hydrogen-bonding sites at the edge sites of the MOF. In MD simulations the basal plane appeared to have fewer adsorption sites due to both void space from the pores and fewer hydrogen-bonding sites compared to the edge plane. We propose that higher Γ_S leads to a greater fouling of the electrode surface by polymerization reactions and other fouling mechanisms. The adsorption parameter $\Delta G°$ for DA on electrode interfaces was identified as the cause of enhanced sensitivity of the {001} interface over the {100} interface as well as the sensitivity enhancement of MOF-based electrodes over GCE. The more exergonic adsorption of DA to the {001}

of the MOF manifested as a higher value for the equilibrium adsorption constant β, which determines electrode coverage at subsaturating concentrations. MD simulations suggested that the {001} interface of the MOF provided more exergonic adsorption sites because of its ability to host both hydrophobic ($\pi-\pi$ bonding) and hydrophilic (H-bonding) interactions.

CONCLUSION

The experimental evidence we presented demonstrates that the confluence of epitaxial self-assembly and anisotropic crystallinity can yield tunable interfaces for electroanalytical applications. This work provides a significant advancement in understanding the electroactive interfaces of anisotropic stacked 2D conductive MOFs for different classes of analytes. We build on previous demonstrations of MOFs for electroanalysis by elucidating fundamental factors that are important in designing effective MOF-based electrodes for analytical applications.

Synthetic access to oriented nanocrystalline facets ({001} and {100}) of two isostructural MOF analogs ($Ni_3(HHTP)_2$ and $Co_3(HHTP)_2$) and their subsequent electrochemical characterization using a series of inorganic and organic redox probes allowed us to identify three key characteristics of the MOFs in electrochemical applications. First, we identified a distinct advantage of the MOFs over bare GCE for enhancing the detection of positively charged analytes, such as DA, while suppressing the interference from negatively charged analytes, such as DOPAC and AA. Second, we discovered electrochemical attributes of the electrolyte−MOF interface at the {100} and {001} family of planes of $M_3(HHTP)_2$. The basal planes belonging to the {001} family of planes of both $Co_3(HHTP)_2$ and $Ni_3(HHTP)_2$ showed slower HETR k^0 for surface-sensitive inorganic probes compared to edge facets belonging to the {100} family of planes. Electrochemical investigations with BROs revealed that the {001} planes were advantageous in adsorption-driven electrochemical processes, such as the oxidation of DA. The herein reported method of integrating {001} oriented $Ni_3(HHTP)_2$ onto GCE allowed the detection of concentrations of DA as low as 9.9 ± 2 nM in PBS. The electrodes also displayed promising sensitivity and selectivity for DA in simulated CSF containing BSA, UA, and glucose at physiologically representative concentrations. Third, we used Langmuir isotherm studies to obtain thermodynamic adsorption parameters of the analytes DA and DOPAC with the {001} and {100} interfaces of $Ni_3(HHTP)_2$, which, when informed by our MD simulations, identified important molecular design criteria for anisotropic MOF systems for the detection of adsorbing analytes.

While this work identifies chemical and structural aspects of MOFs important to their electroanalytical properties, several features and processes remain for further investigation. The limitations of this study are primarily twofold. First, we did not investigate the electron transfer rate or mechanism for BRO detection at MOF electrodes. Oxidative detection of BROs, especially those containing catechol redox centers, commonly relies on proton-coupled electron transfer (PCET) processes.[103,104] Identifying the role of hydrogen bonding, proton transfer, and analyte adsorption in the oxidation of BROs would provide additional insight into the observed benefits of the {001} interface in chemical sensing. Second, we did not examine differences in impedance between the {001} and {100} interfaces for the MOF−GCE heterostructure. Further investigations using electrochemical impedance spectroscopy

could provide more insight into the role of each interface and the heterojunction of MOF−GCE. While these limitations span a range of fundamental to applied aspects, the current work focuses on the experimentally observable differences in 2D conductive MOF orientation in liquid-phase electro-analysis.

In summary, this work provides a crucial experimental and computational methodology for characterizing 2D materials in electrochemical systems. As 2D materials gain prominence in electrochemical applications (i.e., sensing, energy storage, and catalysis), it becomes important to understand how their anisotropy can be controlled and leveraged into advantageous properties. Our demonstration herein, that chemically distinct facets of anisotropic nanocrystalline 2D MOFs can direct electrochemical properties of electrodes by controlling their ensemble orientation through self-assembly, is poised to inform growing areas of electrochemistry and the investigation of important properties of this class of materials.

EXPERIMENTAL METHODS

A complete account of methods, supporting characterization, and experimental results can be found in the Supporting Information.

Synthesis of MOF Nanocrystalline Interfaces. *$M_3(HHTP)_2$ Hydrothermal Method to Obtain Rods.* To prepare MOFs, 0.037 mmol of hexahydroxytriphenylene (12 mg) and 0.074 mmol of metal(II) acetate tetrahydrate (18.4 mg, metal = Co or Ni) were added to a 20 mL scintillation vial. Deionized water (15 mL, 0.005 M [HHTP]) was added, and the vial was loosely capped to allow the exchange of air in the headspace. The reaction mixture was subjected to sonication (5 min) and then heated without stirring (85 °C) overnight (18−24 h). The resulting suspension was characterized by drop-casting onto silicon plates and imaging by SEM and PXRD. Suspensions were stored at 7 °C for up to 2 weeks. Rods were not isolated from the initial reaction mixture but were used as a suspension.

Interfacial Synthesis of $M_3(HHTP)_2$ Films. Into a recrystallizing dish (⌀ = 8 cm) were added metal(II) acetate tetrahydrate (56.5 mg, 0.227 mmol, 2 equiv, metal = Co or Ni) and 100 mL of DI water. Into a vial were added fully reduced HHTP (36.8 mg, 0.113 mmol, 1 equiv) and 20 mL of DI water. The vial was then sonicated for 10 min until a pink/gray suspension was formed. This suspension was poured into the recrystallizing dish containing the $M(OAc)_2$ solution. The reaction was left exposed to air but gently covered to prevent contamination from airborne particles. After 2 h, a thin film visually similar to an oil slick was observed on the surface of the reaction. After an additional 4 h, the film was uncovered and used. Finished films were mounted onto GCE using the Langmuir−Blodgett method.

Electrochemical Experimental Parameters. *Cyclic Voltammetry. Inorganic Probes.* Electrochemical experiments were performed in 0.1 M KCl that had been degassed with N_2. Cyclic voltammograms were collected at nine scan rates starting from the fastest rate and proceeding to the slowest in the following order: 1000, 750, 500, 250, 100, 50, 25, 10, and 5 mV/s. The potential range applied in these experiments was −0.7−0.7 V. Four scans were collected at each scan rate, and the fourth scan from each experiment was plotted on the same plot to characterize the reduction and oxidation events.

Biologically Relevant Organic Probes. Probes in this category were used to determine the performance of these materials in physiologically relevant conditions. Therefore, the electrolyte solution was chosen to be 0.1 M 1× PBS at a pH of 7.4. Cyclic voltammograms were collected at nine scan rates starting from the fastest rate and proceeding to the slowest in the following order: 1000, 750, 500, 250, 100, 50, 25, 10, and 5 mV/s. The potential range applied in these experiments was −0.7−0.7 V, except for the case of K_4IrCl_6, where a potential range of −0.7−1.2 V was used to accommodate the higher oxidation potential of the iridium-based probe. Four scans were collected at each scan rate, and the fourth scan

from each experiment was plotted on the same plot to characterize the reduction and oxidation events.

ASSOCIATED CONTENT

Ⓢ Supporting Information

The Supporting Information is available free of charge at https://pubs.acs.org/doi/10.1021/acsnano.2c02529.

> Experimental details, synthetic details, voltammetric data, scanning electron microscopy (SEM), and X-ray photoelectron spectra (PDF)

AUTHOR INFORMATION

Corresponding Author

Katherine A. Mirica − *Department of Chemistry, Burke Laboratory, Dartmouth College, Hanover, New Hampshire 03755, United States;* Ⓞ orcid.org/0000-0002-1779-7568; Email: katherine.a.mirica@dartmouth.edu

Authors

Robert M. Stolz − *Department of Chemistry, Burke Laboratory, Dartmouth College, Hanover, New Hampshire 03755, United States*

Anna F. Kolln − *Department of Chemistry, Burke Laboratory, Dartmouth College, Hanover, New Hampshire 03755, United States;* Ⓞ orcid.org/0000-0001-8237-5874

Brunno C. Rocha − *Department of Chemical Engineering, Kingsbury Hall, University of New Hampshire, Durham, New Hampshire 03824, United States*

Anna Brinks − *Department of Chemistry, Burke Laboratory, Dartmouth College, Hanover, New Hampshire 03755, United States*

Aileen M. Eagleton − *Department of Chemistry, Burke Laboratory, Dartmouth College, Hanover, New Hampshire 03755, United States*

Lukasz Mendecki − *Department of Chemistry, Burke Laboratory, Dartmouth College, Hanover, New Hampshire 03755, United States*

Harish Vashisth − *Department of Chemical Engineering, Kingsbury Hall, University of New Hampshire, Durham, New Hampshire 03824, United States;* Ⓞ orcid.org/0000-0002-2087-2880

Complete contact information is available at:
https://pubs.acs.org/10.1021/acsnano.2c02529

Author Contributions

R.M.S. and A.F.K. contributed equally to this work. All authors approved the final form of this work.

Notes

The authors declare no competing financial interest.

REFERENCES

(1) Park, S.; Boo, H.; Chung, T. D. Electrochemical Non-Enzymatic Glucose Sensors. *Anal. Chim. Acta* **2006**, *556* (1), 46−57.

(2) Koehne, J. E.; Marsh, M.; Boakye, A.; Douglas, B.; Kim, I. Y.; Chang, S. Y.; Jang, D. P.; Bennet, K. E.; Kimble, C.; Andrews, R.; Meyyappan, M.; Lee, K. H. Carbon Nanofiber Electrode Array for Electrochemical Detection of Dopamine Using Fast Scan Cyclic Voltammetry. *Analyst* **2011**, *136* (9), 1802−1805.

(3) Heineman, W. R.; Kissinger, P. T. Analytical Electrochemistry: Methodology and Applications of Dynamic Techniques. *Anal. Chem.* **1978**, *50* (5), 166−175.

(4) Meng, Z.; Stolz, R. M.; Mendecki, L.; Mirica, K. A. Electrically-Transduced Chemical Sensors Based on Two-Dimensional Nanomaterials. *Chem. Rev.* **2019**, *119* (1), 478−598.

(5) Oja, S. M.; Wood, M.; Zhang, B. Nanoscale Electrochemistry. *Anal. Chem.* **2013**, *85* (2), 473−486.

(6) Hrapovic, S.; Liu, Y.; Male, K. B.; Luong, J. H. Electrochemical Biosensing Platforms Using Platinum Nanoparticles and Carbon Nanotubes. *Anal. Chem.* **2004**, *76* (4), 1083−1088.

(7) Gerhardt, G. A.; Oke, A. F.; Nagy, G.; Moghaddam, B.; Adams, R. N. Nafion-Coated Electrodes with High Selectivity for Cns Electrochemistry. *Brain Res.* **1984**, *290* (2), 390−395.

(8) Yagi, I.; Notsu, H.; Kondo, T.; Tryk, D. A.; Fujishima, A. Electrochemical Selectivity for Redox Systems at Oxygen-Terminated Diamond Electrodes. *J. Electroanal. Chem.* **1999**, *473* (1−2), 173−178.

(9) Katz, E.; Willner, I.; Wang, J. Electroanalytical and Bioelectroanalytical Systems Based on Metal and Semiconductor Nanoparticles. *Electroanalysis* **2004**, *16* (12), 19−44.

(10) Allen, J.; Bard, L. R. F. *Electrochemical Methods*, 2nd ed.; John Wiley & Sons, Inc.: New York, 2001.

(11) Rusling, J. F.; Suib, S. L. Characterizing Materials with Cyclic Voltammetry. *Adv. Mater.* **1994**, *6* (12), 922−930.

(12) Emaminejad, S.; Gao, W.; Wu, E.; Davies, Z. A.; Yin Yin Nyein, H.; Challa, S.; Ryan, S. P.; Fahad, H. M.; Chen, K.; Shahpar, Z.; Talebi, S.; Milla, C.; Javey, A.; Davis, R. W. Autonomous Sweat Extraction and Analysis Applied to Cystic Fibrosis and Glucose Monitoring Using a Fully Integrated Wearable Platform. *Proc. Natl. Acad. Sci. U. S. A.* **2017**, *114* (18), 4625−4630.

(13) Kim, J.; de Araujo, W. R.; Samek, I. A.; Bandodkar, A. J.; Jia, W.; Brunetti, B.; Paixão, T. R. L. C.; Wang, J. Wearable Temporary Tattoo Sensor for Real-Time Trace Metal Monitoring in Human Sweat. *Electrochem. Commun.* **2015**, *51*, 41−45.

(14) Yun, K.-S.; Gil, J.; Kim, J.; Kim, H.-J.; Kim, K.; Park, D.; Kim, M. s.; Shin, H.; Lee, K.; Kwak, J.; Yoon, E. A Miniaturized Low-Power Wireless Remote Environmental Monitoring System Based on Electrochemical Analysis. *Sens. Actuators, B* **2004**, *102* (1), 27−34.

(15) Windmiller, J. R.; Wang, J. Wearable Electrochemical Sensors and Biosensors: A Review. *Electroanalysis* **2013**, *25* (1), 29−46.

(16) Gonon, F. G.; Navarre, F.; Buda, M. J. In Vivo Monitoring of Dopamine Release in the Rat Brain with Differential Normal Pulse Voltammetry. *Anal. Chem.* **1984**, *56* (3), 573−575.

(17) Heffner, T. G.; Hartman, J. A.; Seiden, L. S. Feeding Increases Dopamine Metabolism in the Rat Brain. *Science* **1980**, *208* (4448), 1168−1170.

(18) Alivisatos, A. P.; Andrews, A. M.; Boyden, E. S.; Chun, M.; Church, G. M.; Deisseroth, K.; Donoghue, J. P.; Fraser, S. E.; Lippincott-Schwartz, J.; Looger, L. L.; Masmanidis, S.; McEuen, P. L.; Nurmikko, A. V.; Park, H.; Peterka, D. S.; Reid, C.; Roukes, M. L.; Scherer, A.; Schnitzer, M.; Sejnowski, T. J.; Shepard, K. L.; Tsao, D.; Turrigiano, G.; Weiss, P. S.; Xu, C.; Yuste, R.; Zhuang, X. Nanotools for Neuroscience and Brain Activity Mapping. *ACS Nano* **2013**, *7* (3), 1850−1866.

(19) Gooding, J. J. Nanostructuring Electrodes with Carbon Nanotubes: A Review on Electrochemistry and Applications for Sensing. *Electrochim. Acta* **2005**, *50* (15), 3049−3060.

(20) Huang, J.; Ng, A. L.; Piao, Y.; Chen, C. F.; Green, A. A.; Sun, C. F.; Hersam, M. C.; Lee, C. S.; Wang, Y. Covalently Functionalized Double-Walled Carbon Nanotubes Combine High Sensitivity and Selectivity in the Electrical Detection of Small Molecules. *J. Am. Chem. Soc.* **2013**, *135* (6), 2306−2312.

(21) Tiwari, J. N.; Vij, V.; Kemp, K. C.; Kim, K. S. Engineered Carbon-Nanomaterial-Based Electrochemical Sensors for Biomolecules. *ACS Nano* **2016**, *10* (1), 46−80.

(22) Laurila, T.; Sainio, S.; Caro, M. A. Hybrid Carbon Based Nanomaterials for Electrochemical Detection of Biomolecules. *Prog. Mater. Sci.* **2017**, *88*, 499−594.

(23) Jacobs, C. B.; Peairs, M. J.; Venton, B. J. Review: Carbon Nanotube Based Electrochemical Sensors for Biomolecules. *Anal. Chim. Acta* **2010**, *662* (2), 105−127.

(24) McCreery, R. L. Advanced Carbon Electrode Materials for Molecular Electrochemistry. *Chem. Rev.* **2008**, *108* (7), 2646−2687.

(25) Swiatkowski, A.; Pakula, M.; Biniak, S.; Walczyk, M. Influence of the Surface Chemistry of Modified Activated Carbon on Its Electrochemical Behaviour in the Presence of Lead(Ii) Ions. *Carbon* **2004**, *42* (15), 3057−3069.

(26) Simpson, A.; Pandey, R. R.; Chusuei, C. C.; Ghosh, K.; Patel, R.; Wanekaya, A. K. Fabrication Characterization and Potential Applications of Carbon Nanoparticles in the Detection of Heavy Metal Ions in Aqueous Media. *Carbon* **2018**, *127*, 122−130.

(27) Patel, A. N.; Unwin, P. R.; Macpherson, J. V. Investigation of Film Formation Properties During Electrochemical Oxidation of Serotonin (5-Ht) at Polycrystalline Boron Doped Diamond. *Phys. Chem. Chem. Phys.* **2013**, *15* (41), 18085−18092.

(28) Macpherson, J. V. A Practical Guide to Using Boron Doped Diamond in Electrochemical Research. *Phys. Chem. Chem. Phys.* **2015**, *17* (5), 2935−2949.

(29) Vinokur, N.; Miller, B.; Avyigal, Y.; Kalish, R. Electrochemical Behavior of Boron-Doped Diamond Electrodes. *J. Electrochem. Soc.* **1996**, *143* (10), L238−L240.

(30) Singh, Y. S.; Sawarynski, L. E.; Michael, H. M.; Ferrell, R. E.; Murphey-Corb, M. A.; Swain, G. M.; Patel, B. A.; Andrews, A. M. Boron-Doped Diamond Microelectrodes Reveal Reduced Serotonin Uptake Rates in Lymphocytes from Adult Rhesus Monkeys Carrying the Short Allele of the 5-Httlpr. *ACS Chem. Neurosci.* **2010**, *1* (1), 49−64.

(31) Britto, P. J.; Santhanam, K. S. V.; Ajayan, P. M. Carbon Nanotube Electrode for Oxidation of Dopamine. *Bioelectrochem. Bioenerg.* **1996**, *41* (1), 121−125.

(32) Wang, J. Carbon-Nanotube Based Electrochemical Biosensors: A Review. *Electroanalysis* **2005**, *17* (1), 7−14.

(33) Patel, A. N.; Collignon, M. G.; O'Connell, M. A.; Hung, W. O.; McKelvey, K.; Macpherson, J. V.; Unwin, P. R. A New View of Electrochemistry at Highly Oriented Pyrolytic Graphite. *J. Am. Chem. Soc.* **2012**, *134* (49), 20117−20130.

(34) Ambrosi, A.; Chua, C. K.; Bonanni, A.; Pumera, M. Electrochemistry of Graphene and Related Materials. *Chem. Rev.* **2014**, *114* (14), 7150−7188.

(35) Pumera, M.; Ambrosi, A.; Bonanni, A.; Chng, E. L. K.; Poh, H. L. Graphene for Electrochemical Sensing and Biosensing. *Trends Analyt. Chem.* **2010**, *29* (9), 954−965.

(36) Ambrosi, A.; Chua, C. K.; Latiff, N. M.; Loo, A. H.; Wong, C. H.; Eng, A. Y.; Bonanni, A.; Pumera, M. Graphene and Its Electrochemistry - an Update. *Chem. Soc. Rev.* **2016**, *45* (9), 2458−2493.

(37) Takmakov, P.; Zachek, M. K.; Keithley, R. B.; Walsh, P. L.; Donley, C.; McCarty, G. S.; Wightman, R. M. Carbon Microelectrodes with a Renewable Surface. *Anal. Chem.* **2010**, *82* (5), 2020−2028.

(38) Brownson, D. A. C.; Munro, L. J.; Kampouris, D. K.; Banks, C. E. Electrochemistry of Graphene: Not Such a Beneficial Electrode Material? *RSC Adv.* **2011**, *1*, 6.

(39) Poon, M.; McCreery, R. L. In Situ Laser Activation of Glassy Carbon Electrodes. *Anal. Chem.* **1986**, *58* (13), 2745−2750.

(40) Singh, Y. S.; Sawarynski, L. E.; Dabiri, P. D.; Choi, W. R.; Andrews, A. M. Head-to-Head Comparisons of Carbon Fiber Microelectrode Coatings for Sensitive and Selective Neurotransmitter Detection by Voltammetry. *Anal. Chem.* **2011**, *83* (17), 6658−6666.

(41) Rim, Y. S.; Bae, S. H.; Chen, H.; Yang, J. L.; Kim, J.; Andrews, A. M.; Weiss, P. S.; Yang, Y.; Tseng, H. R. Printable Ultrathin Metal Oxide Semiconductor-Based Conformal Biosensors. *ACS Nano* **2015**, *9* (12), 12174−12181.

(42) Zhao, C.; Liu, Q.; Cheung, K. M.; Liu, W.; Yang, Q.; Xu, X.; Man, T.; Weiss, P. S.; Zhou, C.; Andrews, A. M. Narrower Nanoribbon Biosensors Fabricated by Chemical Lift-Off Lithography Show Higher Sensitivity. *ACS Nano* **2021**, *15* (1), 904−915.

(43) Nakatsuka, N.; Yang, K. A.; Abendroth, J. M.; Cheung, K. M.; Xu, X.; Yang, H.; Zhao, C.; Zhu, B.; Rim, Y. S.; Yang, Y.; Weiss, P. S.; Stojanovic, M. N.; Andrews, A. M. Aptamer-Field-Effect Transistors Overcome Debye Length Limitations for Small-Molecule Sensing. *Science* **2018**, *362* (6412), 319−324.

(44) Cheung, K. M.; Yang, K. A.; Nakatsuka, N.; Zhao, C.; Ye, M.; Jung, M. E.; Yang, H.; Weiss, P. S.; Stojanovic, M. N.; Andrews, A. M. Phenylalanine Monitoring Via Aptamer-Field-Effect Transistor Sensors. *ACS Sens.* **2019**, *4* (12), 3308−3317.

(45) Li, Y.; Ross, A. E. Plasma-Treated Carbon-Fiber Microelectrodes for Improved Purine Detection with Fast-Scan Cyclic Voltammetry. *Analyst* **2020**, *145* (3), 805−815.

(46) McKenas, C. G.; Fehr, J. M.; Donley, C. L.; Lockett, M. R. Thiol-Ene Modified Amorphous Carbon Substrates: Surface Patterning and Chemically Modified Electrode Preparation. *Langmuir* **2016**, *32* (41), 10529−10536.

(47) Biswas, A.; Bayer, I. S.; Biris, A. S.; Wang, T.; Dervishi, E.; Faupel, F. Advances in Top-Down and Bottom-up Surface Nanofabrication: Techniques, Applications & Future Prospects. *Adv. Colloid Interface Sci.* **2012**, *170* (1−2), 2−27.

(48) Isaacoff, B. P.; Brown, K. A. Progress in Top-Down Control of Bottom-up Assembly. *Nano Lett.* **2017**, *17* (11), 6508−6510.

(49) Li, W.; Min, C.; Tan, F.; Li, Z.; Zhang, B.; Si, R.; Xu, M.; Liu, W.; Zhou, L.; Wei, Q.; Zhang, Y.; Yang, X. Bottom-up Construction of Active Sites in a Cu-N4-C Catalyst for Highly Efficient Oxygen Reduction Reaction. *ACS Nano* **2019**, *13* (3), 3177−3187.

(50) Xie, L. S.; Skorupskii, G.; Dincă, M. Electrically Conductive Metal−Organic Frameworks. *Chem. Rev.* **2020**, *120* (16), 8536−8580.

(51) Ko, M.; Mendecki, L.; Mirica, K. A. Conductive Two-Dimensional Metal−Organic Frameworks as Multifunctional Materials. *Chem. Commun. (Camb)* **2018**, *54* (57), 7873−7891.

(52) Wang, N.; Xie, M.; Wang, M.; Li, Z.; Su, X. Uio-66-Nh2Mof-Based Ratiometric Fluorescent Probe for the Detection of Dopamine and Reduced Glutathione. *Talanta* **2020**, *220*, 121352.

(53) Ko, M.; Mendecki, L.; Eagleton, A. M.; Durbin, C. G.; Stolz, R. M.; Meng, Z.; Mirica, K. A. Employing Conductive Metal−Organic Frameworks for Voltammetric Detection of Neurochemicals. *J. Am. Chem. Soc.* **2020**, *142* (27), 11717−11733.

(54) Lu, S.; Jia, H.; Hummel, M.; Wu, Y.; Wang, K.; Qi, X.; Gu, Z. Two-Dimensional Conductive Phthalocyanine-Based Metal−Organic Frameworks for Electrochemical Nitrite Sensing. *RSC Adv.* **2021**, *11* (8), 4472−4477.

(55) Hmadeh, M.; Lu, Z.; Liu, Z.; Gándara, F.; Furukawa, H.; Wan, S.; Augustyn, V.; Chang, R.; Liao, L.; Zhou, F.; Perre, E.; Ozolins, V.; Suenaga, K.; Duan, X.; Dunn, B.; Yamamto, Y.; Terasaki, O.; Yaghi, O. M. New Porous Crystals of Extended Metal-Catecholates. *Chem. Mater.* **2012**, *24* (18), 3511−3513.

(56) Day, R. W.; Bediako, D. K.; Rezaee, M.; Parent, L. R.; Skorupskii, G.; Arguilla, M. Q.; Hendon, C. H.; Stassen, I.; Gianneschi, N. C.; Kim, P.; Dincă, M. Single Crystals of Electrically Conductive Two-Dimensional Metal−Organic Frameworks: Structural and Electrical Transport Properties. *ACS Cent. Sci.* **2019**, *5* (12), 1959−1964.

(57) Ha, D. G.; Rezaee, M.; Han, Y.; Siddiqui, S. A.; Day, R. W.; Xie, L. S.; Modtland, B. J.; Muller, D. A.; Kong, J.; Kim, P.; Dincă, M.; Baldo, M. A. Large Single Crystals of Two-Dimensional Pi-Conjugated Metal−Organic Frameworks Via Biphasic Solution-Solid Growth. *ACS Cent. Sci.* **2021**, *7* (1), 104−109.

(58) Tan, T. T.; Reithofer, M. R.; Chen, E. Y.; Menon, A. G.; Hor, T. S.; Xu, J.; Chin, J. M. Tuning Omniphobicity Via Morphological Control of Metal−Organic Framework Functionalized Surfaces. *J. Am. Chem. Soc.* **2013**, *135* (44), 16272−16275.

(59) Virmani, E.; Rotter, J. M.; Mahringer, A.; von Zons, T.; Godt, A.; Bein, T.; Wuttke, S.; Medina, D. D. On-Surface Synthesis of Highly Oriented Thin Metal−Organic Framework Films through Vapor-Assisted Conversion. *J. Am. Chem. Soc.* **2018**, *140* (14), 4812−4819.

(60) Rubio-Gimenéz, V.; Galbiati, M.; Castells-Gil, J.; Almora-Barrios, N.; Navarro-Sanchez, J.; Escorcia-Ariza, G.; Mattera, M.; Arnold, T.; Rawle, J.; Tatay, S.; Coronado, E.; Martí-Gastaldo, C. Bottom-up Fabrication of Semiconductive Metal−Organic Framework Ultrathin Films. *Adv. Mater.* **2018**, *30*, 10.

(61) Huang, Z.; Zhang, L.; Cao, P.; Wang, N.; Lin, M. Electrochemical Sensing of Dopamine Using a Ni-Based Metal−-Organic Framework Modified Electrode *Ionics* **2021**, *27*, 1339.

(62) Abrori, S. A.; Septiani, N. L. W.; Hakim, F. N.; Maulana, A.; Suyatman, S.; Nugraha, S.; Anshori, I.; Yuliarto, B. Non-Enzymatic Electrochemical Detection for Uric Acid Based on a Glassy Carbon Electrode Modified with MOF-71. *IEEE Sensors Journal* **2020**, 1−1.

(63) Fang, J.-J.; Yang, N.-N.; Gao, E.-Q. Making Metal−Organic Frameworks Electron-Deficient for Ultrasensitive Electrochemical Detection of Dopamine. *Electrochem. Commun.* **2018**, *89*, 32−37.

(64) Qiao, Y.; Liu, Q.; Lu, S.; Chen, G.; Gao, S.; Lu, W.; Sun, X. High-Performance Non-Enzymatic Glucose Detection: Using a Conductive Ni-MOF as an Electrocatalyst. *J. Mater. Chem. B* **2020**, *8* (25), 5411−5415.

(65) Ko, M.; Aykanat, A.; Smith, M. K.; Mirica, K. A. Drawing Sensors with Ball-Milled Blends of Metal−Organic Frameworks and Graphite. *Sensors (Basel)* **2017**, *17*, 10.

(66) Smith, M. K.; Mirica, K. A. Self-Organized Frameworks on Textiles (Soft): Conductive Fabrics for Simultaneous Sensing, Capture, and Filtration of Gases. *J. Am. Chem. Soc.* **2017**, *139* (46), 16759−16767.

(67) Mahringer, A.; Jakowetz, A. C.; Rotter, J. M.; Bohn, B. J.; Stolarczyk, J. K.; Feldmann, J.; Bein, T.; Medina, D. D. Oriented Thin Films of Electroactive Triphenylene Catecholate-Based Two-Dimensional Metal−Organic Frameworks. *ACS Nano* **2019**, *13* (6), 6711−6719.

(68) Butler, D.; Moore, D.; Glavin, N. R.; Robinson, J. A.; Ebrahimi, A. Facile Post-Deposition Annealing of Graphene Ink Enables Ultrasensitive Electrochemical Detection of Dopamine. *ACS Appl. Mater. Interfaces* **2021**, *13* (9), 11185−11194.

(69) Xu, J.; Yokota, Y.; Wong, R. A.; Kim, Y.; Einaga, Y. Unusual Electrochemical Properties of Low-Doped Boron-Doped Diamond Electrodes Containing sp^2 Carbon. *J. Am. Chem. Soc.* **2020**, *142* (5), 2310−2316.

(70) Chen, P.; McCreery, R. L. Control of Electron Transfer Kinetics at Glassy Carbon Electrodes by Specific Surface Modification. *Anal. Chem.* **1996**, *68* (22), 3958−3965.

(71) Moo, J. G.; Ambrosi, A.; Bonanni, A.; Pumera, M. Inherent Electrochemistry and Activation of Chemically Modified Graphenes for Electrochemical Applications. *Chem. Asian J.* **2012**, *7* (4), 759−770.

(72) Guell, A. G.; Ebejer, N.; Snowden, M. E.; McKelvey, K.; Macpherson, J. V.; Unwin, P. R. Quantitative Nanoscale Visualization of Heterogeneous Electron Transfer Rates in 2D Carbon Nanotube Networks. *Proc. Natl. Acad. Sci. U. S. A.* **2012**, *109* (29), 11487−11492.

(73) Si, B.; Song, E. Recent Advances in the Detection of Neurotransmitters. *Chemosensors* **2018**, *6*, 1.

(74) Goldstein, D. S.; Holmes, C.; Lopez, G. J.; Wu, T.; Sharabi, Y. Cerebrospinal Fluid Biomarkers of Central Dopamine Deficiency Predict Parkinson's Disease. *Parkinsonism Relat Disord* **2018**, *50*, 108−112.

(75) Nagatsu, T. The Catecholamine System in Health and Disease -Relation to Tyrosine 3-Monooxygenase and Other Catecholamine-Synthesizing Enzymes. *Proc. Jpn. Acad. Ser. B Phys. Biol. Sci.* **2006**, *82* (10), 388−415.

(76) Adler, L. E.; Gerhardt, G. A.; Franks, R.; Baker, N.; Nagamoto, H.; Drebing, C.; Freedman, R. Sensory Physiology and Catecholamines in Schizophrenia and Mania. *Psychiatry Res.* **1990**, *31* (3), 297−309.

(77) Seet, R. C.; Lee, C. Y.; Lim, E. C.; Tan, J. J.; Quek, A. M.; Chong, W. L.; Looi, W. F.; Huang, S. H.; Wang, H.; Chan, Y. H.; Halliwell, B. Oxidative Damage in Parkinson Disease: Measurement Using Accurate Biomarkers. *Free Radic. Biol. Med.* **2010**, *48* (4), 560−566.

(78) Becker, B. F. Towards the Physiological Function of Uric Acid. *Free Radic. Biol. Med.* **1993**, *14* (6), 615−631.

(79) Du, J.; Cullen, J. J.; Buettner, G. R. Ascorbic Acid: Chemistry, Biology and the Treatment of Cancer. *Biochim. Biophys. Acta* **2012**, *1826* (2), 443−457.

(80) Sajid, M.; Baig, N.; Alhooshani, K. Chemically Modified Electrodes for Electrochemical Detection of Dopamine: Challenges and Opportunities. *Trends Analyt. Chem.* **2019**, *118*, 368−385.

(81) Ou, Y.; Buchanan, A. M.; Witt, C. E.; Hashemi, P. Frontiers in Electrochemical Sensors for Neurotransmitter Detection: Towards Measuring Neurotransmitters as Chemical Diagnostics for Brain Disorders. *Anal. Methods* **2019**, *11* (21), 2738−2755.

(82) Schildkraut, J. J. The Catecholamine Hypothesis of Affective Disorders: A Review of Supporting Evidence. *Am. J. Psychiatry* **1965**, *122* (5), 509−522.

(83) Kim, Y. R.; Bong, S.; Kang, Y. J.; Yang, Y.; Mahajan, R. K.; Kim, J. S.; Kim, H. Electrochemical Detection of Dopamine in the Presence of Ascorbic Acid Using Graphene Modified Electrodes. *Biosens. Bioelectron.* **2010**, *25* (10), 2366−2369.

(84) Bacil, R. P.; Chen, L.; Serrano, S. H. P.; Compton, R. G. Dopamine Oxidation at Gold Electrodes: Mechanism and Kinetics near Neutral pH. *Phys. Chem. Chem. Phys.* **2020**, *22* (2), 607−614.

(85) Queiroz, D. F.; Dadamos, T. R. L.; Machado, S. A. S.; Martines, M. A. U. Electrochemical Determination of Norepinephrine by Means of Modified Glassy Carbon Electrodes with Carbon Nanotubes and Magnetic Nanoparticles of Cobalt Ferrite. *Sensors (Basel)* **2018**, *18*, 4.

(86) Maldonado, S.; Morin, S.; Stevenson, K. J. Electrochemical Oxidation of Catecholamines and Catechols at Carbon Nanotube Electrodes. *Analyst* **2006**, *131* (2), 262−267.

(87) Hawley, M. D.; Tatawawadi, S. V.; Piekarski, S.; Adams, R. N. Electrochemical Studies of the Oxidation Pathways of Catecholamines. *J. Am. Chem. Soc.* **1967**, *89* (2), 447−450.

(88) Wierzbicka, E.; Szultka-Młyńska, M.; Buszewski, B.; Sulka, G. D. Epinephrine Sensing at Nanostructured Au Electrode and Determination Its Oxidative Metabolism. *Sens. Actuators, B* **2016**, *237*, 206−215.

(89) Pisoschi, A. M.; Pop, A.; Serban, A. I.; Fafaneata, C. Electrochemical Methods for Ascorbic Acid Determination. *Electrochim. Acta* **2014**, *121*, 443−460.

(90) Wang, Y. The Electrochemistry of Uric Acid at a Gold Electrode Modified with L-Cysteine, and Its Application to Sensing Uric Urine. *Microchimica Acta* **2011**, *172* (3−4), 419−424.

(91) Van Wazer, J. R.; Callis, C. F. Metal Complexing by Phosphates. *Chem. Rev.* **1958**, *58* (6), 1011−1046.

(92) Chakravarti, S. N.; Talibudeen, O. Phosphate Equilibria in Acid Soils. *Journal of Soil Science* **1962**, *13* (2), 231−240.

(93) Nicholson, R. S.; Shain, I. Theory of Stationary Electrode Polarography. Single Scan and Cyclic Methods Applied to Reversible, Irreversible, and Kinetic Systems. *Anal. Chem.* **1964**, *36* (4), 706−723.

(94) Klinger, R. J.; Kochi, J. K. Electron-Transfer Kinetics from Cyclic Voltammetry. Quantitative Description of Electrochemical Reversibility. *J. Phys. Chem.* **1981**, *85* (12), 1731−1741.

(95) Lavagnini, I.; Antiochia, R.; Magno, F. An Extended Method for the Practical Evaluation of the Standard Rate Constant from Cyclic Voltammetric Data. *Electroanalysis* **2004**, *16* (6), 505−506.

(96) Yao, M. S.; Lv, X. J.; Fu, Z. H.; Li, W. H.; Deng, W. H.; Wu, G. D.; Xu, G. Layer-by-Layer Assembled Conductive Metal−Organic Framework Nanofilms for Room-Temperature Chemiresistive Sensing. *Angew. Chem. Int. Ed. Engl.* **2017**, *56* (52), 16510−16514.

(97) Zhang, G.; Cuharuc, A. S.; Guell, A. G.; Unwin, P. R. Electrochemistry at Highly Oriented Pyrolytic Graphite (HOPG): Lower Limit for the Kinetics of Outer-Sphere Redox Processes and General Implications for Electron Transfer Models. *Phys. Chem. Chem. Phys.* **2015**, *17* (17), 11827−11838.

(98) Bressers, P. M. M. C.; Pagano, S. A. S. P.; Kelly, J. J. Ferricyanide Reduction as a Probe for the Surface Chemistry of Silicon in Aqueous Alkaline Solutions. *J. Electroanal. Chem.* **1995**, *391* (1−2), 159−168.

(99) Huang, L.; Deng, M.; Fang, Y.; Li, L. Dynamic Changes of Five Neurotransmitters and Their Related Enzymes in Various Rat Tissues Following Beta-Asarone and Levodopa Co-Administration. *Exp. Ther. Med.* **2015**, *10* (4), 1566−1572.

(100) Swenson, H.; Stadie, N. P. Langmuir's Theory of Adsorption: A Centennial Review. *Langmuir* **2019**, *35* (16), 5409−5426.

(101) Lim, G. N.; Ross, A. E. Purine Functional Group Type and Placement Modulate the Interaction with Carbon-Fiber Microelectrodes. *ACS Sens.* **2019**, *4* (2), 479−487.

(102) Todorov, I. T.; Smith, W.; Trachenko, K.; Dove, M. T. Dl_Poly_3: New Dimensions in Molecular Dynamics Simulations Via Massive Parallelism. *J. Mater. Chem.* **2006**, *16*, 1911−1918.

(103) Lin, Q.; Li, Q.; Batchelor-McAuley, C.; Compton, R. G. Two-Electron, Two-Proton Oxidation of Catechol: Kinetics and Apparent Catalysis. *J. Phys. Chem. C* **2015**, *119* (3), 1489−1495.

(104) Iuga, C.; Alvarez-Idaboy, J. R.; Vivier-Bunge, A. Ros Initiated Oxidation of Dopamine under Oxidative Stress Conditions in Aqueous and Lipidic Environments. *J. Phys. Chem. B* **2011**, *115* (42), 12234−12246.

▣ Recommended by ACS